APPLIED SCIENCES AND ENGINEERING

# A wearable biomechanical system for medical evaluation of soft tissue disorders

**Min-Seung Jo[1]†, Hee-Sup Shin[2]†, Jin-Tae Kim[3]†, Shupeng Li[4], Sonwoo Jung[5,6], Jungyeon Kim[3], Tae Wan Park[1], Jodi L. Johnson[7,8,9,10], Carrie Richardson[1,11], Eseosa Olive Osaghae[11], Kyoung-Ho Ha[1,12], Hyosik Park[1,13], Josif Bozovic[1,14], Winnie Sung[1,14], Jaewon Lim[3], Sammer Marzouk[1], Yujin Choi[1], Sofia Natasha Guzman[15], Bridget Christina Groble[15], Shuai Xu[1,16], Fredrick Wigley[17], Jae-Young Yoo[18]*, Yonggang Huang[5,19,20]*, Ann Marie Flores[7,10,14,21]*, John A. Rogers[1,4,13,19,22]***



**Evaluating soft tissue elasticity provides critical biomechanical insights essential for the precise characterization of various physiological and pathological conditions. Here, we present the clinical validation of a wireless, compact wearable system designed for direct, location-specific monitoring of the elastic modulus of the skin and underlying tissues via vibro-rotational biomechanical dynamics. Validated by computational models and experiments, the device uses a tunable skin interface to enable depth-controlled measurements across diverse anatomical sites. Two human subject studies, one involving patients with cancer-related lymphedema and the other involving patients with systemic scleroderma, yield data that correlate with standard clinical metrics. This technology offers the potential for longitudinal assessments in these and other contexts, in both clinical and home settings.**

## INTRODUCTION

The mechanical properties of the skin and underlying soft tissues serve as comprehensive indicators of a range of clinical conditions, capturing alterations that arise from physiological variations and pathological processes. In particular, changes in elasticity measured from the surface of the skin (its stress-strain behavior) result not only to superficial alterations due to aging (*1*), fibrosis (*2*), and recurrent infection (*3*) but also to vascular and systemic conditions, including altered muscle tone (*4*), edema (*5*), heart failure (*6*), and protein wasting enteropathies (*7*). Timely and reliable assessment of the mechanical properties of soft tissue is largely limited to the clinical exam; delayed recognition of abnormalities can lead to worsening infection (e.g., cellulitis), skin breakdown (e.g., venous leg ulcerations from lower extremity edema), excessive scarring or fibrosis (e.g., rapidly progressive scleroderma), developing functional impairment, increased treatment burden, and reduced quality of life (*8*, *9*). Therefore, early detection and continuous monitoring of mechanical changes can be essential to prevent these avoidable outcomes. Current medical systems for evaluating structural skin abnormalities are, however, often involve bulky instrumentation for spot checks, and require expert interpretation (*10*–*12*), while manual techniques like the pinch test typically offer limited resolution and demand trained evaluators (*13*). A quantitative data-driven approach is desirable for accurate and accessible evaluation of biomechanical changes.

Quantification of skin biomechanics can be accomplished with a range of established techniques, each based on the assessment of tissue deformation and elastic response under mechanical or acoustic loading. Examples include devices based on suction (*14*, *15*), indentation (*16*, *17*), elastography (*18*), and vibration-based dynamic profiling (*19*–*22*). The first two techniques, while widely used, suffer from uncertainties due to variabilities in the orientation of force delivery at the skin interface. Also, these methods focus primarily on superficial tissue behavior. Elastography enables assessments at deep tissue locations, but the performance can be strongly influenced by subtle variations in surface curvature and fine-scale structural heterogeneity, thereby limiting real-time monitoring to anatomically regular regions. Vibrational acoustic methods quantify mechanical responses in the frequency domain under well-controlled sensor-skin contact, supporting real-time evaluations of tissue properties with minimal interference from interface conditions (*19*). Recent progress in these techniques enables biomechanical measurements across superficial and deep tissue layers by controlled propagation of oscillatory deformations into underlying structures (*20*). While robust vibrational actuators and different monitoring components can capture dynamic acoustic waves at deep tissue ranges, several implementation aspects require attention to evolve these systems into clinically applicable, user-friendly platforms. Some systems measure the vibrational response

[1]Querrey-Simpson Institute for Bioelectronics, Northwestern University, Evanston, IL, USA. [2]School of Science and Engineering, University of Missouri Kansas City, Kansas City, MO, USA. [3]Department of Mechanical Engineering, Pohang University of Science and Technology, Pohang, Republic of Korea. [4]Department of Civil and Environmental Engineering, Northwestern University, Evanston, IL, USA. [5]Center for Nanoparticle Research, Institute for Basic Science (IBS), Seoul, Republic of Korea. [6]School of Chemical and Biological Engineering, Institute of Chemical Processes, Seoul National University, Seoul, Republic of Korea. [7]Robert H. Lurie Comprehensive Cancer Center, Feinberg School of Medicine, Northwestern University, Chicago, IL, USA. [8]Department of Dermatology, Feinberg School of Medicine, Northwestern University, Chicago, IL, USA. [9]Department of Pathology, Feinberg School of Medicine, Northwestern University, Chicago, IL, USA. [10]Department of Medical Social Sciences, Feinberg School of Medicine, Northwestern University, Chicago, IL, USA. [11]Division of Rheumatology, Northwestern University Feinberg School of Medicine, Chicago, IL, USA. [12]Department of Bio and Brain Engineering, Korea Advanced Institute of Science and Technology, Daejeon, Republic of Korea. [13]Department of Energy Science and Engineering, Daegu Gyeongbuk Institute of Science and Technology (DGIST), Daegu, Republic of Korea. [14]Department of Biomedical Engineering, Northwestern University, Evanston, IL, USA. [15]Department of Physical Therapy and Human Movement Sciences, Feinberg School of Medicine, Northwestern University, Chicago, IL, USA. [16]Sibel Health Inc., Chicago, IL, USA. [17]Division of Rheumatology, Johns Hopkins University School of Medicine, Baltimore, MD, USA. [18]Department of Semiconductor Convergence Engineering, Sungkyunkwan University, Suwon, Republic of Korea. [19]Department of Mechanical Engineering, Northwestern University, Evanston, IL, USA. [20]Department of Materials Science and Engineering, Northwestern University, Evanston, IL, USA. [21]Cancer Survivorship Institute, Robert H. Lurie Comprehensive Cancer Center of Northwestern University, Chicago, IL, USA. [22]Department of Neurological Surgery, Feinberg School of Medicine, Northwestern University, Chicago, IL, USA.
*Corresponding author. Email: jy.yoo@skku.edu (J.-Y.Y.); y-huang@northwestern.edu (Y.H.); ann.flores@northwestern.edu (A.M.F.); jrogers@northwestern.edu (J.A.R.)
†These authors contributed equally to this work.

at a location offset from the mechanical excitation point (*21*, *22*), resulting in a spatial mismatch that introduces uncontrolled variability due to wave propagation through intervening tissues. In addition, these technologies currently lack demonstrations of clinical utility, and they also require further engineering work to yield compact form factors suitable for routine use in continuous or ambulatory diagnostic settings.

This paper presents a biomechanical diagnostic system that exploits a compact, wireless interface for the direct, location-specific quantification of skin elastic modulus, serving as a foundation for continuous point-of-care assessments. The device captures vibro-rotational motions via an integrated actuator and inertial measurement unit (IMU), translating mechanical coupling into tissue data. A tunable contact interface modulates the effective depth of this coupling, providing depth-resolved sensitivity to subsurface tissue structures—essential for isolating specific anatomical layers—as verified by image-based analysis of vibration profiles in skin phantoms. These capabilities in deep tissue interaction can reveal regional differences in dermal, subcutaneous fat, and muscle thickness while also capturing alterations that originate from underlying tissue structures. Clinical evaluation with patients with lymphedema ($n = 28$) verifies the clinical utility of the system by quantifying mechanical responses associated with lymphatic fluid accumulation and edema. The results align with measurements performed using the medical standard for bioimpedance spectroscopy (SOZO by ImpediMed), and they outperform evaluations with a commercial indentation device (ElastiMeter; Delfin Technologies). Furthermore, the quantitative assessment of patients with scleroderma reveals that skin modulus values determined with this device correspond to established qualitative clinical benchmarks, thereby establishing the utility in monitoring skin disease progression. Given that alterations in skin elasticity reflect inflammatory activity (*3*) and impaired epidermal differentiation (*23*), the platform introduced here can serve as a practical tool capable of supporting early detection of a range of skin and soft tissue pathologies.

## RESULTS

### Wearable, wireless skin modulus sensor

Figure 1A schematically illustrates the eccentric rotating motor-based skin modulus (ESM) sensor, designed as a convenient mechanomedical diagnostic device with wireless charging and communication capabilities. The sensor consists of two main parts: (i) an island that integrates an eccentric rotating mass (ERM) motor with an IMU that directly tracks accelerations associated with resulting oscillatory motions, and (ii) a main body that contains a lithium-polymer (Li-Po) battery, along with a system-on-chip (SoC) and peripheral electronics that control operation, acquire data, and support wireless communication with a smart device via Bluetooth low energy (BLE) protocols. During measurement, the sensor interfaces with the skin by securing both the motor and the main body using medical-grade double-sided adhesive, thereby minimizing the need for secondary user involvement [e.g., manual holding of probes, as required in conventional systems (*16*, *17*)]. A serpentine conductive path connecting the island to the main body does not adhere to the skin, enabling the ERM to operate with minimal mechanical interference from other components. This configuration also facilitates customization of the sensor for specific diagnostic applications by varying the size of the interchangeable disc-shaped skin-contact head (hereafter called the head of the device) (Fig. 1B). A skin-safe silicone shell encapsulates the circuit board and the Li-Po battery, ensuring electrical insulation while leaving the motor exposed to deliver vibro-rotational actuation to the skin. With a high degree of stretchability of the serpentine interconnect and the soft encapsulating shell, the device supports stable and robust operation under complex mechanical deformations, including stretching, bending, and twisting (Fig. 1C). Simulations based on finite element analysis (FEA) for the structural parameters of flexible printed circuit board (fPCB; PCBWay) indicate that even under substantial deformation—such as 25% stretching, bending with a 5-mm radius, or 360° twisting—the induced strains remain below the fracture thresholds of the key constituent materials [Cu elongation at break ~5% (*24*); fig. S1].

The vibro-rotational dynamics of the motor change with the mechanical properties of the skin due to the mechanical coupling at the interface, thereby serving as the basis for estimation of the skin modulus. The ERM motor generates vibro-rotational motion by spinning an unbalanced weight, creating a centrifugal force. As this force vector rotates, it produces multidirectional movements, especially with forces parallel to the skin surface. The skin modulus, which correlates with stiffness, influences the mechanical response to vibration, leading to changes in the steady-state vibration amplitude and frequency. High modulus values result in high vibration frequencies and low amplitudes due to an increased mechanical resistance to motor-induced displacement (Fig. 1D). The dynamics also depend on skin thickness, specifically the penetration of vibrational motions into the depth of the tissue. Large areas of contact between the skin and the head lead to spatially extended distributions of shear forces, thereby inducing tissue deformations at depths up to 40 mm (Fig. 1E). This dependence can be exploited to allow for mechanical diagnostics both at deep tissue locations—where changes associated with lymphatic or vascular abnormalities may arise—and at shallow regions. In particular, with a simple change in contact area, the target depth can be adjusted from ~5 to 40 mm, enabling the detection of modulus changes, including those associated with muscle alterations, at different body locations and at different characteristic depths.

Realization of this sensor in a compact, integrated form with a customized user-interface (UI) software and robust, low-power electronics allows not only for utility in medical clinics but also potentially in the home. Consuming less than 5 mW in standby, the ERM motor provides strong haptic interaction and continuous operation for more than 30 min ($\approx 3.6 \times 10^5$ vibration cycles) without electrical or mechanical degradation. For typical measurement times of ~1 s, a single charge allows for ~180 measurements (Fig. 1F). Even after $10^6$ rotation cycles on a skin phantom, vibration frequency and amplitude remain consistent, confirming reliable operation without fPCB fatigue (fig. S1C). The system is wirelessly rechargeable via near-field communication protocols. As illustrated in the block diagram in Fig. 1G, the BLE chip acquires acceleration data at a high sampling rate (~800 Hz) via a serial peripheral interface (SPI) communication approach, which corresponds to more than four times the maximum motor vibration frequency (~192 Hz). The UI controls motor operation via a general purpose input-output interface and an N-type transistor, as the basis for setting the duration of vibration. The UI directly processes the acquired data (Fig. 1H), tracks the sinusoidal acceleration waveform, and extracts the vibrating frequency using fast Fourier transform. The algorithm then fits the acceleration amplitude with a nonlinear least-squares method to estimate the displacement amplitude.

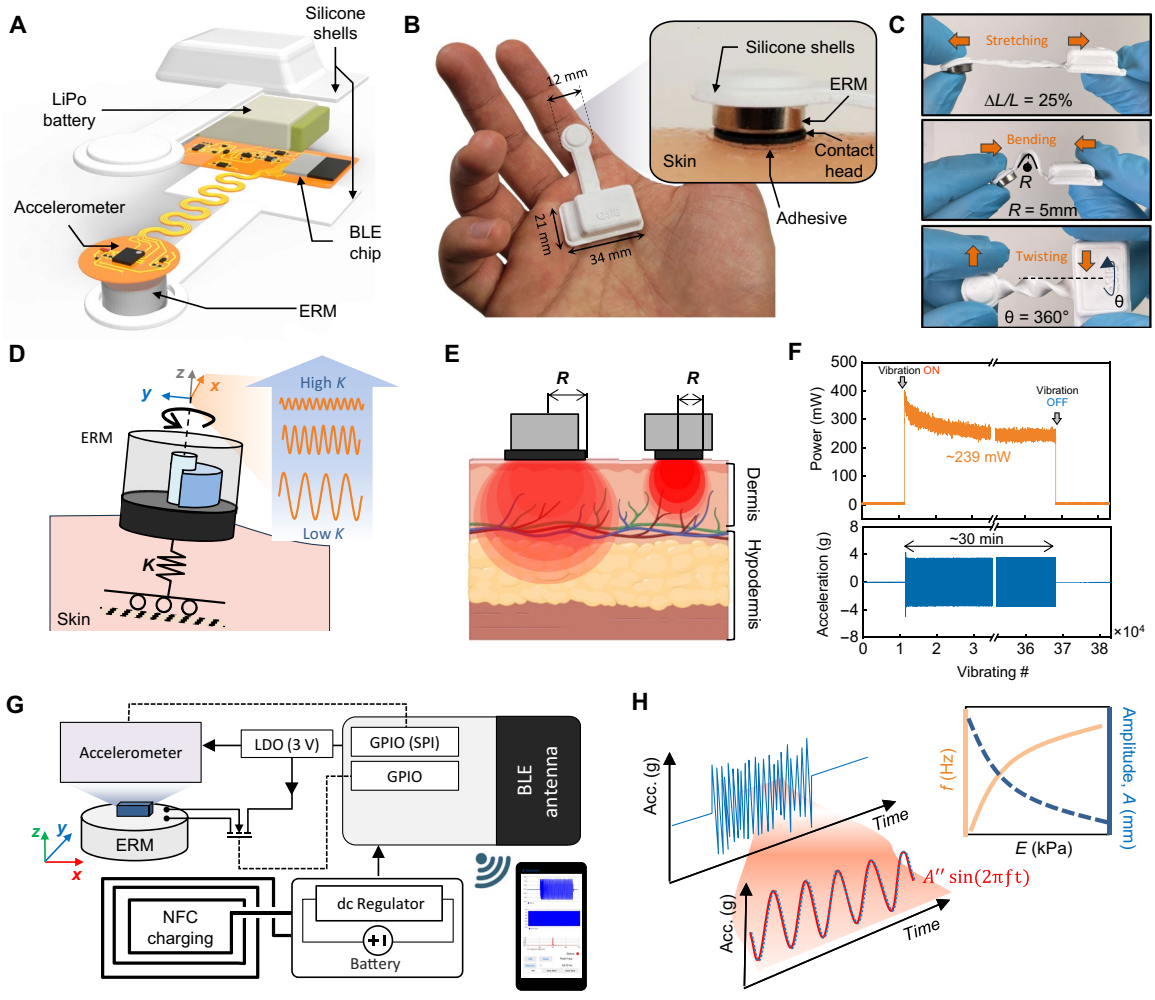


**Fig. 1. Wearable wireless skin modulus sensor.** (**A**) Schematic illustration of the skin modulus sensor, which operates a vibrating eccentric rotating motor while measuring acceleration using an embedded IMU. (**B**) Photograph of the device; the inset shows a side view while attached to the skin. (**C**) Photographs of the sensor under mechanical loading. (**D**) Working principle of the actuator vibration on the skin—the vibration frequency and amplitude vary depending on the modulus of the contacted material. (**E**) Contact area–dependent propagation of vibration when attached to the skin. *R* denotes the radius of the circular head. Created in BioRender. Rogers, J. (2026) https://BioRender.com/sn7gsp0. (**F**) Operational power consumption (top) and acceleration (bottom) over 3.6 × $10^4$ cycles during 30 min of motor vibration. (**G**) Block diagram illustrating the operation. (**H**) Accelerometer signal processing for direct monitoring of actuator-induced vibration via sine wave analysis. LDO, Low-Dropout regulator; GPIO, general purpose input-output; NFC, near-field communication; Acc., Acceleration.

## Analytical and experimental validation of mechanical dynamics

An analytical model developed under steady-state conditions enables quantitative assessment of skin stiffness during ERM vibration and facilitates the determination of skin modulus. Applying a direct current to the ERM drives the eccentric mass to rotate about the output shaft, which reaches a constant angular velocity under steady-state conditions. As shown in Fig. 2A, the acceleration in this case exhibits sinusoidal waveforms along all directions (*x* and *y*: normal and along fPCB, respectively; *z*: normal to the surface of the skin). The displacement amplitude ($A$) follows from the acceleration amplitude ($A''$) based on the harmonic motion identity [$A = A''/(2\pi f)^2$], as validated through point tracking with a high-speed camera (fig. S2). The negligibly small values in the *z* direction, which follow from the constraint imposed by attachment of the ERM to the skin, allow for an analytical model that focuses on in-plane vibrations on the skin surface. The in-plane (*x*-*y*) stiffness of the system includes contributions from both fPCB and skin. The fPCB provides notable stiffness along the *y* direction, leading to a reduced displacement amplitude compared to the *x* direction (normal to the fPCB). The displacement in the *x* direction is linear in applied force with constant stiffness within the physiological range of a few to several hundred kilopascal (figs. S3 and S4 and note S1). A linear proportional relation between the skin stiffness and modulus, obtained by FEA, thus provides a quantitative basis for determining the skin modulus (figs. S5 to S7 and note S2) (*25*, *26*).

Skin phantoms formed with polydimethylsiloxane (PDMS) enable validation of the analytical model. Figure 2B presents the measured frequencies and amplitudes across phantoms with varying moduli, resulting from use of different ratios of softening additives and curing agents (Materials and Methods and fig. S8). Comparisons between experimental and analytic results indicate excellent correlation (Fig. 2C and note S3). Furthermore, the results are the same before and after

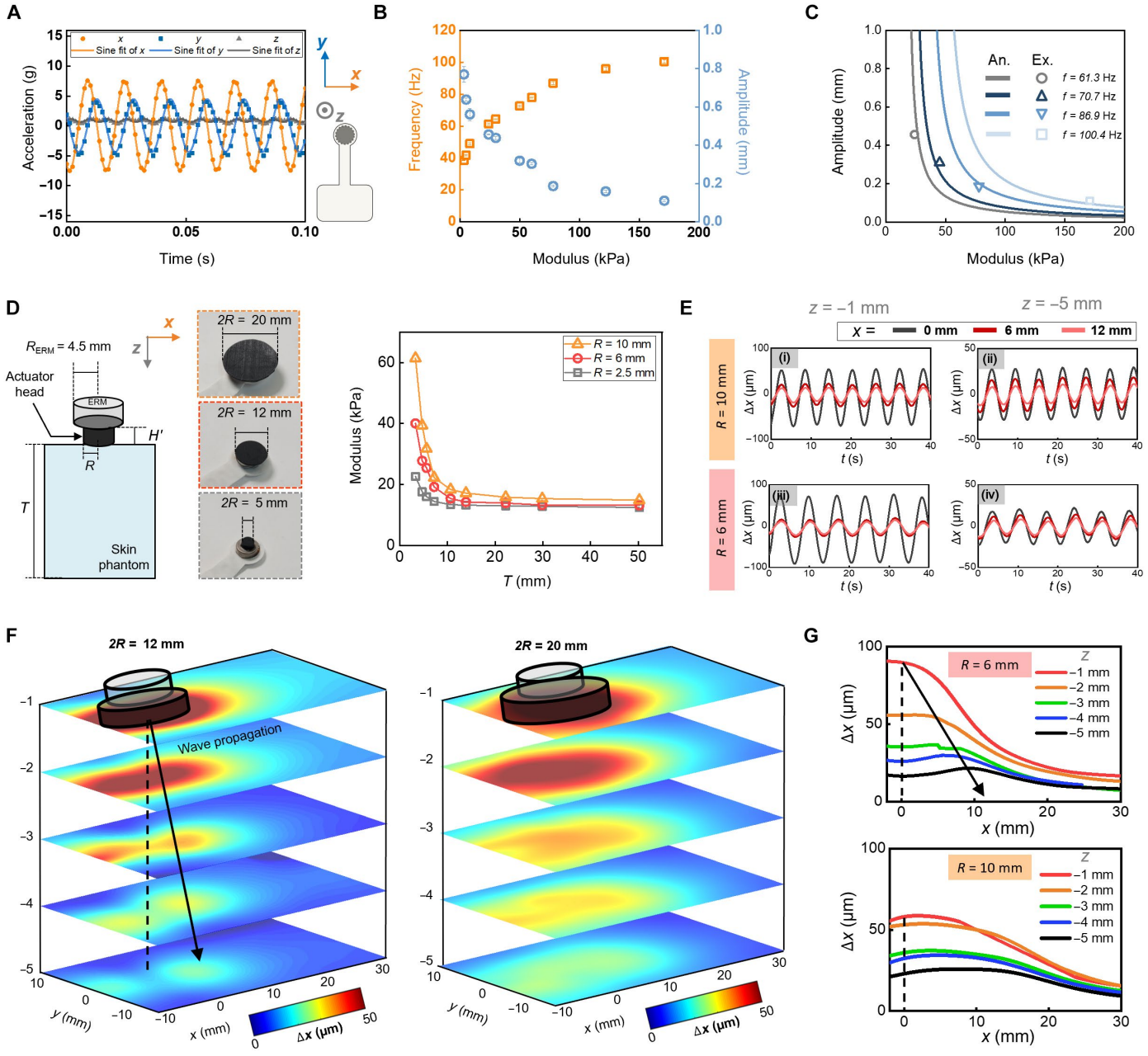


**Fig. 2. Device characterization and analytical verification.** (**A**) Real-time acceleration data associated with motor vibration along three axes. (**B**) Measured vibration frequency and amplitude across skin phantoms with varying moduli. (**C**) On the basis of a subset of the data in (B), comparison between the analytical results (An.) and experimental results (Ex.) of skin modulus variation with vibration amplitude (*A*) at four frequencies (*f*) for an ERM without a head ($R = 4.5$ mm, $H' = 0$ mm). Here, *R* and *H*′ denote the radius and height of the head, respectively. (**D**) Modulus values obtained by using heads of different sizes on skin phantoms with varying depths (*T*). (**E**) Experimentally measured real-time amplitude displacement ($\Delta x$) of the skin phantom under vibration for the *R*10 and *R*6 heads at $z = -1$ mm and $z = -5$ mm. (**F**) Two-dimensional (2D) contours along the depth direction under vibration for *R*6 and *R*10. The arrow denotes the line extending from the center to the maximum *x*-displacement point. (**G**) Depth-dependent maximum vibration displacement along $y = 0$ corresponding to (F).

incorporating the soft encapsulation shell, as expected due to its low stiffness and small thickness (<0.5 mm) layer (fig. S9).

## Characterization of depth-resolved dynamics

Varying the contact area of the head, the component in direct contact with the skin, substantially alters the depth-dependent dynamics, as qualitatively described in the previous section. Experiments to characterize these mechanics use heads with radii of 2.5 mm (*R*2.5), 6 mm (*R*6), and 10 mm (*R*10) applied to skin phantoms with various moduli. The theoretical moduli predicted from the measured frequency and amplitude agree with the experimentally measured moduli, with less than 10% error (fig. S10). Evaluations of depth-dependent mechanical interactions use skin phantoms with an identical modulus of 13 kPa but varying thicknesses (*T*) fixed onto a rigid substrate.

The measurements yield the apparent modulus as a function of $T$ (Fig. 2D). Reducing $T$ increases the apparent modulus as expected due to the mechanical influence of the underlying rigid substrate ($E >>$ 1 GPa). As the thickness increases, the apparent modulus progressively reaches a saturation point, converging toward a value characteristic of an elastic half-space of the skin phantom. An *R*2.5 head applied to a phantom with $T = 3.3$ mm yields a modulus 1.7-fold higher than the saturation value, which occurs at $T \sim 10$ mm. An *R*10 head produces a fourfold increase and saturates at $T \sim 40$ mm. Thus, larger contact areas engage deeper layers, resulting in higher apparent moduli at lower phantom thicknesses and a greater thickness to reach saturation. FEA confirms that shear forces induced by larger heads promote deeper, more monotonic displacements (fig. S11), with an interacting depth of ~4*R*.

Depth-resolved measurements with three-dimensional digital image correlation [3D DIC (*27*)] directly reveal the displacement fields (fig. S12). A comparison of lateral displacement amplitudes at depths of 1 and 5 mm indicates that the *R*6 head induces larger displacements near the surface but a more rapid decrease with depth than those with the *R*10 head (Fig. 2E). With a *R*6 head, displacements near the surface are large but attenuate rapidly with depth, resulting in nonuniform, irregular patterns of deformation at deeper layers [Fig. 2, F (left) and G (top)]. By comparison, the *R*10 head generates smaller surface displacements that propagate more uniformly and monotonically into deeper regions, yielding a nearly linear attenuation profile [Fig. 2, F (right) and G (bottom)], further validated using porcine subcutaneous tissue (fig. S13). These experimental trends match theoretical expectations, where reduced out-of-plane deformation with larger contact areas support smoother propagation into deeper layers. At very small contact areas (e.g., *R*2.5), excessive local out-of-plane deformation and torque—arising from Euler's disk-like 3D motion induced by the ERM (*28*)—lead to unstable coupling and loss of contact with the skin, underscoring a stability limit for effective actuation. Collectively, these results demonstrate mechanisms by which head geometry governs both the effective interaction depth and the stability of vibration-tissue coupling.

## Human skin modulus measurement

During the measurement, the actuator initially exhibits vibrations with relatively large amplitudes, which then settle into a steady-state oscillation with uniform frequency and amplitude. By collecting data after the initial settling period (~0.5 s), the resulting modulus values are invariant to the measurement duration (Fig. 3A). In addition, although the baseline acceleration shifts with device orientation relative to the gravitational vector, the vibration frequency and amplitude remain consistent, independent of the device-skin interface angle (fig. S14) and alignment between the vibration direction and gravity (fig. S15). With these considerations, the skin modulus can be determined with high repeatability precision (<5%) across different devices, locations, and phantoms (Fig. 3B and fig. S16). In practice, robust adhesion to the skin yields consistent results, regardless of the presence of hair and hydration (fig. S17). In addition, measurement failure primarily arises from sensor detachment due to handling-related issues. In these cases, the vibration signal exhibits a distributed frequency spectrum, which can be quantified using a spectral energy concentration ratio to assess measurement reliability (fig. S18).

Figure 3C shows photographs of representative body locations and corresponding measurement outcomes obtained from different individuals. The skin consists of the epidermis, which typically measures 1 to 4 mm in thickness, followed by the dermis and, at a deeper level, the hypodermis that transitions into a subcutaneous fat layer (*29*). Use of the *R*2.5 head leads to measurements dominated by the superficial skin layers. The *R*6 head interacts with comparatively deep tissues. Measurements in this case lead to modulus values less than 10 kPa, comparable to those of subcutaneous fat (*15*, *30*). In contrast, the *R*2.5 head shows modulus values larger than 20 kPa, representing values between those of the superficial skin and fat. Regions of the body with a relatively thick dermis or abundant subcutaneous fat, such as the thigh, abdomen, calf, and upper arm, lead to distinct differences between shallow (*R*2.5) and deep (*R*6) measurements. By contrast, regions where the dermis is thin and/or locations of bony prominence exhibit relatively high modulus values, with little difference between the results obtained with these two heads, as expected.

Deep tissue interaction with the ESM sensor enables detection of the stiffening effect induced by contraction of the underlying musculature. As muscle tension rises during contraction (stressing) of the wrist flexors in the forearm, sensors targeting shallow and deep tissues capture the corresponding increases in modulus (Fig. 3D). Notably, while the modulus determined with the *R*2.5 head increases by approximately 1.2 times, the modulus obtained with the *R*6 head exhibits nearly a threefold increase, reflecting stronger interaction with the underlying muscle layer. The latter setup allows real-time tracking of changes in modulus associated with both muscle activity and skin stretching, as demonstrated during stressing and relaxing of the quadriceps while sitting and standing (Fig. 3, E and F). Here, skin tension alone can contribute to an increase in effective modulus (fig. S19), and the observed changes reflect the combined effects of both skin tension and muscle contraction. Furthermore, posture-dependent measurements indicate that orientation relative to gravity can act as a confounding factor (fig. S20, A to C); however, posture changes without muscle involvement result in negligible changes in the measured modulus (fig. S20, D and E).

Use of multiple sensors enables real-time monitoring of spatial distributions of soft-tissue tension over large areas. An important consideration is in the potential for cross-talk between adjacent sensors (Fig. 3G and fig. S21). Typically, for separations larger than 10 mm, the effect on the resulting modulus value is less than 10% for both the forearm and upper arm, owing to the intrinsically small displacement amplitudes, <1 mm (fig. S22). Wirelessly connecting a 4 by 2 array of sensors simultaneously allows for real-time mapping of the upper back skin in both relaxed and posture-induced skin-stretched states, as illustrated in Fig. 3H. As shown with the *R*2.5 head, the stretched state of the skin that results from bending forward leads to an increase in the effective modulus (Fig. 3I). Evaluation with the *R*6 head yields similar results (fig. S23, A and B) but with larger increases in modulus due to the greater depth of the measurement. This outcome is expected from localized muscular protrusion and differential tissue response during forward bending: The upper back skin flattens as the superficial skin extends, whereas the lower back region displays localized bulging due to erector spinae muscle contraction (*31*). The multisensor array further enables real-time tracking of posture-dependent changes between stretched and relaxed states (fig. S23, C and D) and can resolve asymmetric responses, such as localized muscle activation during unilateral arm elevation (fig. S24).

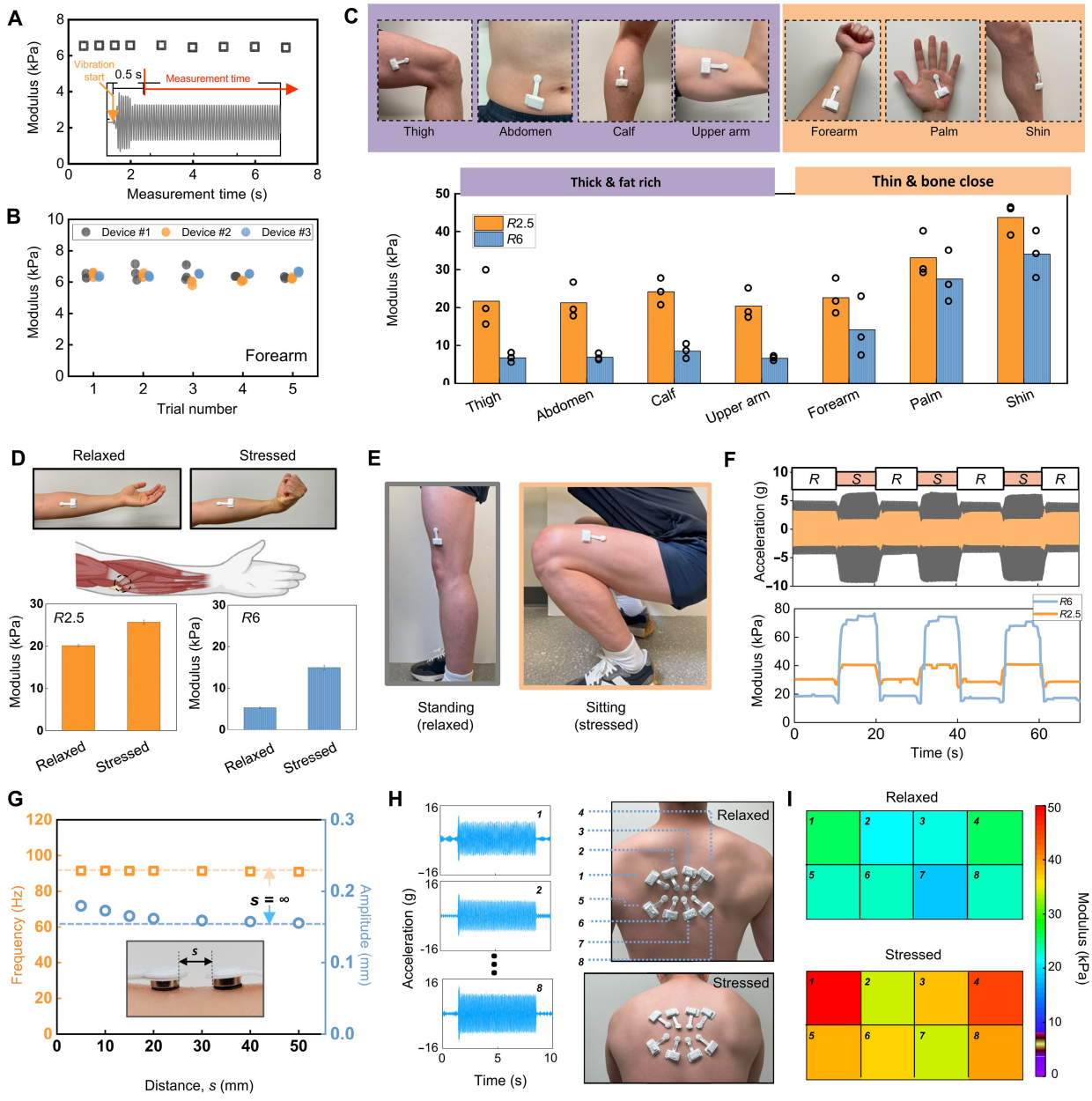


**Fig. 3. Measurement results on human skin.** (**A**) Time-dependent skin modulus during processing. (Inset) Vibrational amplitude over the measurement time. (**B**) Reliability test through repeated measurements at the same body location, with three measurements per trial for each device. (**C**) Skin modulus measured at different body locations using *R*2.5 and *R*6 heads. Each dot represents the average of three measurements, and the bars indicate the overall average across participants ($n = 3$). (**D**) Skin modulus of the forearm under relaxed and contracted muscle conditions using *R*2.5 and *R*6 heads. Created in BioRender. Rogers, J. (2026) https://BioRender.com/sn7gsp0. (**E**) Optical images of the thigh muscle in standing and sitting postures. (**F**) Corresponding real-time acceleration (top) and calculated modulus (bottom). (**G**) Vibration coupling test with varying distances (*s*) between sensors. (**H**) Optical photograph and measurement results from multiple sensors mounted on the back. (**I**) Large-area spatial mapping of skin modulus on the back during relaxed (top) and contracted (bottom) muscle states.

## Mechano-diagnostic application for early detection of patients with lymphedema

Measuring changes in the mechanical properties of the deep skin allows for an assessment of abnormalities that result from diseases that originate beneath the superficial skin. As an example, lymphedema results from the abnormal accumulation of lymphatic fluid in the subcutaneous tissue, with resultant swelling, inflammation, and, in advanced stages, fibrosis. These changes alter the mechanical properties in a corresponding manner (*32*). Cancer-related lymphedema (CRL) is typically caused by either surgical removal of the underlying lymph nodes or radiation therapy—supportive care is the only available treatment and requires lifelong monitoring and management by patients and clinical specialists. Self-management is critical to prevent and control infection (cellulitis), worsening edema,

and irreversible fibrosis. In this context, our device offers notable advantages over conventional approaches (table S1), owing to its fully integrated actuator-sensor system with an embedded battery and wireless circuitry, which together provide high wearability and high measurement repeatability. These features are critical for achieving true clinical feasibility, as they enable continuous and reliable assessment of deep skin mechanical changes.

Demonstrations of the diagnostic functionality involve studies of patients with unilateral upper extremity lymphedema classified as stage 1 or stage 2 [stage 1: early, reversible swelling; stage 2: a more advanced stage with persistent swelling and early fibrosis, serving as progression indicators (*33*)]. Measurements target five anatomical sites on the arm where lymphatic fluid accumulates: two on the forearm, two on the upper arm, and one on the axillary region (Fig. 4A). A commercial device (Elastimeter, Delfin Technologies) also measures skin stiffness at the same body locations for cross-validation. In addition, estimates of arm volume follow from circumferential measurements taken at 40-mm intervals along the limb, which is a common approach for limb volumetry (*34*). Beginning at the wrist and ending at the axillary fold, each segment between adjacent measurements can be approximated as a truncated cone, and the total volume corresponds to the sum of all segmental volumes. Bioimpedance spectroscopy using the Food and Drug Administration–approved device (SOZO by ImpediMed) provides reference data for early lymphedema evaluation and is recommended for early detection of breast CRL (*35*). Standardized measurement conditions in a fully relaxed state minimize artifacts from stretching of the skin or activation of the muscle. Furthermore, the average and deviation of three measurements at each location ensure and assess repeatability. Comparison with commercial stiffness measuring devices reveals consistent trends. Comparatively low modulus values occur in the axillary region and proximal forearm near the elbow, and high values occur in the lateral upper arm and distal forearm near the wrist (Fig. 4B).

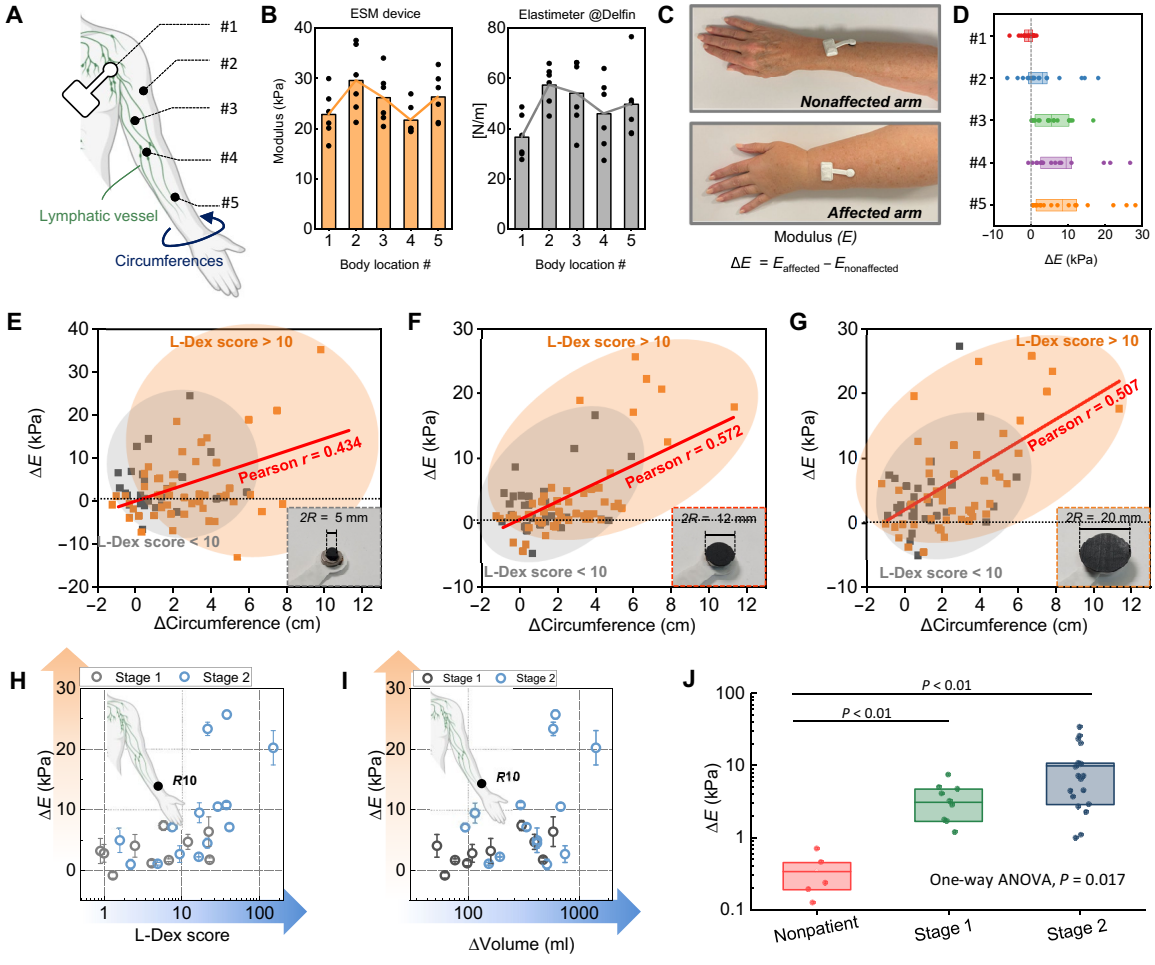


**Fig. 4. Clinical application to patients with lymphedema.** (**A**) Schematic illustration of body measurement points. Created in BioRender. Rogers, J. (2026) https://BioRender.com/sn7gsp0. (**B**) Comparison with a commercial device (ElastiMeter, Delfin Technologies) across different body locations ($n = 14$). (**C**) Representative photograph showing both arms of a lymphedema patient. (**D**) Modulus differences between affected and unaffected arms presented as 25 to 75% percentiles with a mean line for patients with an L-Dex score >10, measured across contact areas (*R6* and *R10*) ($n = 28$). (**E** to **G**) Modulus differences according to arm circumference at measurement locations using ESM devices with different head diameters: (E) *R2.5*; (F) *R6*; (G) *R10* ($n = 28$). Individual results with error bars from repeated measurements are shown. Distal forearm [location #5 in (A)] modulus difference (**H**) as a function of L-Dex score. Each dot corresponds to an individual patient. (**I**) As a function of inter-arm volume difference. (**J**) Comparison of modulus changes in healthy controls ($n = 5$) and patients with lymphedema at stage 1 ($n = 10$) and stage 2 ($n = 18$), presented as 25 to 75% percentiles with a mean line.

The difference in the modulus between the affected and nonaffected arms of a given individual represents an indicator of lymphedema severity and progression. As shown in the photograph of Fig. 4C, the affected arm exhibits volumetric expansion caused by accumulated lymphatic fluid. This expansion induces tensile strain in the skin, resulting in an increased effective modulus, as analytically interpreted on the basis of an incompressible material model (figs. S25 and S26 and note S4) (*36*). In the hyperelastic skin model, the modulus increases with strain; thus, greater swelling produces larger modulus changes and more pronounced differences at higher severity levels. Increased swelling results in a corresponding increase in circumferential tensile strain within the skin. When the deformation of the hyperelastic skin exceeds its elastic limit, the modulus increases with strain (note S4). When comparing the change in modulus ($\Delta E$) at each location, a clear increase appears in the regions of thin skin (distal upper arm and forearm), where stress alterations due to swelling are expected to be greater, compared with the regions of thicker skin (armpit and proximal upper arm) (Fig. 4D and fig. S27). This observation is related to fact that interstitial fluid accumulation—and the resulting skin swelling—typically begins in the distal regions of the extremities due to gravitational effects (*37*).

At these regions of thin skin, measurements using three different contact areas enable assessments of the skin through different depths. The results indicate that changes in modulus correlate in an expected manner with changes in circumference and L-Dex score (Fig. 4, E to G), which reflects an increase in tissue fluid caused by lymphatic fluid accumulation. A L-Dex bioimpedance score greater than 10 is considered indicative of clinically severe lymphedema (*35*). Measurements with the *R*2.5 head target the superficial skin. The modulus values in this case exhibit a relatively low correlation (Pearson coefficient, $r = 0.434$) with the L-Dex score, likely because lymphedema-associated fibrosis requires further progression to reach the skin surface. In contrast, measurements with the *R*6 and *R*10 heads show relatively high correlations (Pearson coefficient, $r > 0.5$), as their more comprehensive interaction with deep skin layers captures the mechanical changes more effectively. This result is consistent with changes in modulus that quantitatively reflect the degree of swelling and tissue fluid. At each location, differences in modulus with respect to the change in circumference reveal that both proximal and distal forearms exhibit a strong correlation with these parameters (fig. S28).

For each individual, correlations between the L-Dex score—measured at the distal forearm (*R*10, targeting deep-tissue monitoring)—and the corresponding volume appear in Fig. 4 (H and I) (data from other body locations are in fig. S29). Patients with an L-Dex score >10 and a volume difference ($\Delta V$) > 200 ml consistently exhibit high modulus values in the affected arm with high correlation. Correlations observed here exceed those obtained with the commercial devices (fig. S30 and table S2). Multiple repeated measurements demonstrate strong consistency. Within-individual deviations are only 0.12 of that observed across individuals. This finding suggests potential uses as an early diagnostic indicator. In particular, the difference in modulus between the arms of healthy subjects is 0.34 kPa {95% confidence interval (CI): [0.05, 0.63]}. In patients, this difference increases across the stages averaging 3.09 kPa (95% CI: [1.43, 4.75]) in stage 1 and 9.9 kPa (95% CI: [5.07, 14.65]) in stage 2. A one-way analysis of variance (ANOVA) indicates a significant overall group effect ($F = 4.69$, $P = 0.017$), supporting that the levels are statistically distinguishable. The lymphedema patients' demographics are summarized in table S3.

## Mechano-physiological differentiation of pathological skin in patients with scleroderma

The technology also supports quantitative monitoring in the context of other health conditions. An example is in scleroderma—characterized by edema, volumetric expansion, and skin fibrosis. Currently, the standard method for assessing severity is the pinch test [modified Rodnan skin score (mRSS)] (*38*), which rates skin thickness on a semiquantitative scale of 0 to 3. This method is subjective, lacks sensitivity to small but clinically meaningful changes, and requires highly experienced, trained evaluators. To explore the utility of the technology introduced here, evaluations consist of measurements at representative anatomical sites used in clinical assessments: the index finger, the hand, and the forearm (Fig. 5A). Unlike lymphedema, scleroderma presents heterogeneity across patients and body locations, encompassing both limited and diffuse subtypes rather than localized to a single side. Therefore, the study compares affected sites of patients against both their own unaffected sites and a nonpatient control group, with measurements performed bilaterally (left and right) at each location. All affected areas (index finger, dorsum of the hand, and forearm) exhibit elevated modulus values ranging from 50 to 100 kPa compared to



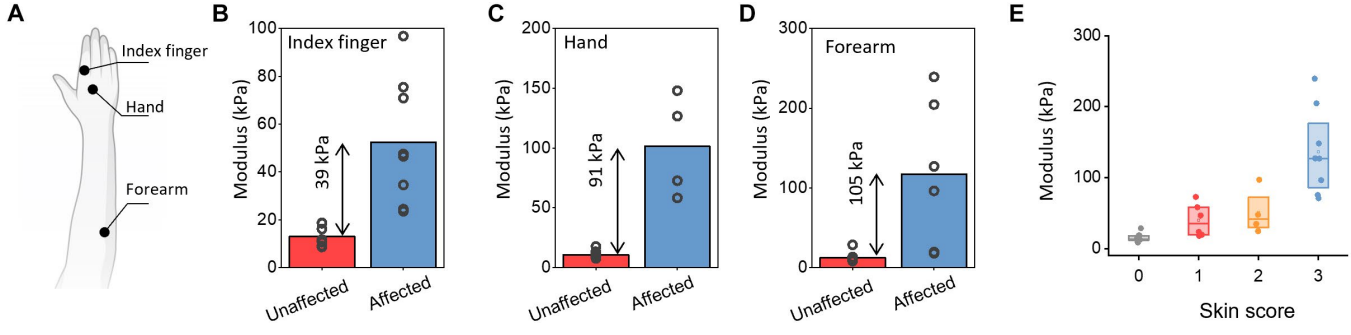


**Fig. 5. Clinical application to scleroderma patients.** (**A**) Schematic illustration of measurement locations. Created in BioRender. Rogers, J. (2026) https://BioRender.com/sn7gsp0. (**B** to **D**) Comparison of modulus data at unaffected and affected areas from left and right sides for each body location forearm (nonpatient $n = 3$, patient $n = 5$): (B) index finger; (C) hand; (D) forearm. (**E**) Modulus values versus skin score (mRSS) for patients across the three locations, presented as 25 to 75% percentiles with a mean line ($n = 5$).

those of unaffected participants (Fig. 5, B to D). The differences are pronounced and distinguishable relative to unaffected areas, each of which show values below 20 kPa. The average increase is thus more than a factor of three, with a maximum increase that exceeds an order of magnitude. Furthermore, skin modulus values show a clear increasing trend with increasing mRSS scores, indicating the potential of this method as a more objective and sensitive indicator of disease progression (Fig. 5E).

## DISCUSSION

The modulus-sensing system presented here enables accurate, reliable measurements with a compact, wireless platform, for continuous and localized monitoring of skin and soft tissue mechanics. The results serve as the basis for automated disease diagnosis and monitoring by leveraging biomechanical signatures of a range of human pathologies. Direct tracking of vibro-rotational motions captures interactions between the induced oscillations of an actuator component and the contacting tissue, to allow for precise quantification from superficial regions of the skin to deep tissue locations. This adaptability can be configured to address requirements in specific tissue alterations of interest, thereby accommodating variations in skin thickness across body locations and enabling assessment of muscle tone and abnormalities originating outside of a primary dermatological cause. High-resolution assessments at single or multiple locations simultaneous across various body regions bridge mechanical outcomes to clinically interpretable metrics.

Specific examples of clinical applications presented here include accurate tracking of multiple stages of lymphedema and the spatial distribution of scleroderma. Because lymphedema requires frequent monitoring and long-term management, the ability of this system to operate as a home care unit substantially enhances its clinical utility. Bioimpedance spectroscopy is commonly used for early-stage assessment, but commercial devices that rely on this mechanism are expensive, restricted mainly to the upper and lower extremities, and typically limited to clinical settings that require trained professionals for testing and interpretation. Although the condition can also affect the legs, perineum, trunk, face, head, and neck, patients with cancers in these regions are difficult to evaluate with current methods. Consequently, the ability of the small, wearable device introduced here to be placed across diverse body locations offers a distinct advantage for broader patient populations. Particularly for scleroderma, where assessments across multiple anatomical sites are essential, this expertise-independent monitoring capability effectively facilitates follow-up care, serving as a quantitative alternative that overcomes the limited resolution of the mRSS. Given that both diseases demonstrated here are difficult to fully recover from and require continuous management, there is a growing need to adopt sensing approaches for longitudinal monitoring in patients with chronic conditions during follow-up. By tracking temporal changes over several months during routine visits, this system is intended to support prospective validation of disease progression and treatment response. The implications of this work expand to a broad range of additional clinical use cases. For instance, lower extremity cellulitis is misdiagnosed at a rate of 30% leading up to 130,000 unnecessary hospitalizations yearly—objective assessment of unilateral skin induration may help increase diagnostic certainty (*39*). Both venous stasis and deep vein thromboses lead to lower extremity swelling requiring frequent application and use of compression stocking therapy. A wearable sensor that is able to alert patients and clinicians of worsening edema objectively would enable treatment management and potentially prevent costly venous leg ulcers, which now account for $2.5 to $3.5 billion in yearly US health expenditures (*40*). Potential also exists in the characterization of inflammatory skin lesions by detecting mechanical markers such as tissue induration during crusting and desquamation. Extending to deeper tissue dynamics, the system can track muscle hypertrophy, subcutaneous fat variations, and tensioning patterns indicative of postural alignment, as a practical tool for monitoring daily wellness and rehabilitation progression.

This simple, fast, easy-to-use, cost-effective monitoring device offers the ability to return quantitative data to health care providers to guide early diagnosis and detect deterioration. The device also represents a potential paradigm shift for assessing the efficacy of investigational therapeutics targeting fibrotic conditions—rather than using subjective and insensitive rating scales like the Rodnan skin thickness test, objective outputs from the device can reveal clinical benefit sooner and with more confidence as a digital biomarker. Applicability extends beyond clinical applications to aesthetics as an objective assessment of skin age and wrinkle formation. Potential also exists in the characterization of inflammatory skin lesions by detecting mechanical markers such as tissue induration during edema, crusting, and desquamation. Extending to deeper tissue dynamics, the system can track muscle hypertrophy, subcutaneous fat variations, and tensioning patterns indicative of postural alignment, as a practical tool for monitoring daily wellness and rehabilitation progression.

## MATERIALS AND METHODS

### Wireless embedded system design

The modulus measurement unit integrates a Bluetooth SoC and associated hardware. The IMU (BMI160, Bosch) records acceleration at 800 Hz with a range of up to 156.8 m/s$^2$ from the attached round section connected through serpentine electrodes and transmits acceleration data using the SPI communication protocol. A 3.7-V, 200-mAh Li-Po battery powers the device. The integrated coil with a 13.56-MHz resonance frequency, along with the voltage rectifier and regulator, enables wireless charging even after encapsulation. Another voltage regulator continuously powers the sensor and motor components during Bluetooth communication. The Bluetooth SoC controls an N-channel FET to turn the motor power on/off from the voltage regulator.

### Fabrication of the skin modulus sensor

A fPCB with copper electrical traces (18-μm thick) on a polyimide film (100-μm thick) provides mechanical support and electrical connections. The board consists of two sections: a rectangular section that integrates BLE communication, charging, and power management components, and a round section that integrates the inertial sensor and an light-emitting diode (VLMS1500-GS08, Vishay Semiconductors) that serves as an indicator of actuator operation. A serpentine interconnect links the two sections. An actuating motor (VW0934AB001G; Vybronics) with 9 mm in diameter mounts onto the round section of the fPCB. A silicone elastomer (Dragon Skin 10 SLOW, SMOOTH-ON, mixed with silicone thinner at a 5:1 ratio) encapsulates the fPCB and the Li-Po battery, with a punched opening accommodating the protruding actuator. The elastomer layer, with a thickness as low as 0.5 mm, covers only the external electrical pads without adding mechanical tension that could interfere with

the vibration. After encapsulation, a 3D-printed head with varying contact areas mounts on top of the actuator.

### Preparation and characterization of artificial skin phantom

Skin phantoms with various modulus values used the components of the silicone elastomer precursor (PDMS, Sylgard 184 and silicone thinner) mixed at different ratios. The mixtures were poured into either a petri dish or a jar to a thickness greater than 50 mm, followed by degassing for 30 min in vacuum. Curing occurred in an oven at 75°C for 24 hours. After curing, the phantoms were cut into samples with lengths of 20 mm and cross-sectional areas smaller than 10 $mm^2$. Tensile stresses and elongations were evaluated using a dynamic mechanical analyzer (RSA-G2 Solids Analyzer, TA Instruments) in combination with a Mark-10 force-torque measurement unit. Figure S8 presents the mixing ratios and the modulus values. The ESM device evaluated the modulus values of the phantoms with its rectangular fPCB section and battery fixed to the base using double-sided adhesive (2477p, 3M) while minimizing tension and compression on the serpentine interconnect. The heads attached to the PDMS phantom using same double-sided adhesive tape, and the system captured inertial motions during operation. The device wirelessly transmitted the data to a mobile iOS application on an iPhone, which determined and displayed the vibration frequency and amplitude.

### Finite element analysis

The commercial software ABAQUS was used to investigate the mechanical behavior of the ERM-based skin modulus sensor on a skin phantom. A model of the ERM, with its upper surface connected to an fPCB wire, was created to assess the device's mechanical characteristics under various external loads, including stretching, bending, and twisting (see fig. S1). In addition, another model of the ERM connected to an fPCB and mounted on a skin phantom was used to examine how the fPCB wire affects the system's stiffness when subjected to displacements in the $x$ and $y$ directions (refer to figs. S3 and S4). Furthermore, a model of the ERM with heads mounted on a skin phantom was used to analyze how the contact areas influence the depth of skin deformation (see fig. S11). This model also allowed for the investigation of the impact of geometric parameters (the thickness and radius of the head) and skin modulus ($E$) on skin stiffness (see fig. S7). The thin fPCB—composed of copper (Cu) and polyimide (PI) layers—was modeled with composite shell elements (S4R), while the skin phantom, ERM, and other components of devices are modeled using hexahedral elements (C3D8R). The minimum element size for the fPCB mesh was set to 1/20 of its width, and the mesh was highly refined in the head contact area. Mesh convergence was verified for all cases. The elastic modulus ($E$) and Poisson's ratio ($\nu$) are $E_{skin}$ = 13.8 kPa, $\nu_{skin} = 0.5$, $E_{Cu} = 119$ GPa, $\nu_{Cu} = 0.3$, $E_{ERM} = 113$ GPa, $\nu_{ERM} = 0.34$, $E_{PI} = 2.5$ GPa, and $\nu_{PI} = 0.34$.

### 3D digital image correlation

Three sets of 3D DIC experiments characterized the 3D deformations of skin phantoms modulated by an ERM actuator embedded in a modulus sensor device, using three different head types: $R = 2.5$ mm, $R = 6$ mm, and $R = 10$ mm. Two high-speed cameras (2048 × 512 in resolution; HT-2000M, Emergent) with 35-mm imaging lenses (F1.4 manual focus; Kowa) captured the 3D displacements and positioned at an inclination angle of 15°. The system acquired images at a sampling rate of 700 frames per second and processed the captured data using the open-source 3D DIC software MultiDIC (*41*). To investigate the effect of depth on surface deformation, five types of skin phantoms were prepared by embedding black speckles at varying depths (1 to 5 mm from the surface) within a 10-mm-thick transparent silicon elastomer (PDMS). A single ERM actuator operating at 3.0 V was mounted on top of the phantom skin via the modulus sensor device. High-speed cameras positioned below the phantom skin captured both the regions directly beneath the device and the surrounding areas. The measurement volume was set to 45 mm by 30 mm by 10 mm for all experiments. To achieve high-resolution, accurate wave-displacement characteristics, the DIC subset radius and spacing were set at 20 and 10 pixels, respectively, resolving more than 3000 grids.

### Human clinical studies

For lymphedema studies, researchers recruited patients who had previously been diagnosed with nonmetastatic cancer and developed lymphedema affecting the upper extremity (anterior axillary fold, medial upper arm, forearm, and/or hand). Researchers collected data only after obtaining participants' informed consent. The measurement process included assessments using the SOZO device (Bioimpedance measurement unit; by ImpediMed), circumferential measurements, the modulus sensor, and two commercial stiffness sensors (ElastiMeter and SkinFibroMeter; Delfin Technologies). Researchers performed all measurements while participants rested their arms on a desk in a fully relaxed position, minimizing muscle activation or movement interference. For scleroderma studies, during the measurement process, patients were seated in a chair reclined at a 30° angle with arms supported by a pillow to maintain a fully relaxed state, minimizing muscle tension. The measurements were performed on the same sites used for mRSS evaluations. The Northwestern University International Review Board approved these studies (Institutional Review Board numbers STU00222670 and STU00223146). Before participation, all individuals underwent a comprehensive informed consent process where the study's purpose, the investigational nature of the wearable sensors, potential risks such as skin irritation, and data confidentiality protocols were explained in detail. Participants were given the opportunity to ask questions and were informed of their right to withdraw from the study at any time without penalty before providing their written or secure online consent.

## Supplementary Materials

**This PDF file includes:**

Supplementary Notes S1 to S4
Figs. S1 to S30
Tables S1 to S3
References

## REFERENCES

1. S. Diridollou, V. Vabre, M. Berson, L. Vaillant, D. Black, J. Lagarde, J. Grégoire, Y. Gall, F. Patat, Skin ageing: Changes of physical properties of human skin in vivo. *Int. J. Cosmet. Sci.* **23**, 353–362 (2001).
2. M. L. Crichton, X. Chen, H. Huang, M. A. Kendall, Elastic modulus and viscoelastic properties of full thickness skin characterised at micro scales. *Biomaterials* **34**, 2087–2097 (2013).
3. M. S. Shutova, W.-H. Boehncke, Mechanotransduction in skin inflammation. *Cells* **11**, 2026 (2022).
4. J.-L. Gennisson, T. Deffieux, E. Macé, G. Montaldo, M. Fink, M. Tanter, Viscoelastic and anisotropic mechanical properties of in vivo muscle tissue assessed by supersonic shear imaging. *Ultrasound Med. Biol.* **36**, 789–801 (2010).
5. R. Killaars, T. L. Penha, E. Heuts, R. van der Hulst, A. Piatkowski, Biomechanical properties of the skin in patients with breast cancer-related lymphedema compared to healthy individuals. *Lymphat. Res. Biol.* **13**, 215–221 (2015).

6. Z. Abassi, E. E. Khoury, T. Karram, D. Aronson, Edema formation in congestive heart failure and the underlying mechanisms. *Front. Cardiovasc. Med.* **9**, 933215 (2022).
7. A. Ozen, M. J. Lenardo, Protein-losing enteropathy. *N. Engl. J. Med.* **389**, 733–748 (2023).
8. S. Thomis, N. Devoogdt, B. Bechter-Hugl, I. Fourneau, Early disturbance of lymphatic transport as a risk factor for the development of breast-cancer-related lymphedema. *Cancers* **15**, 1774 (2023).
9. J. P. Gross, C. M. Lynch, A. M. Flores, S. W. Jordan, I. B. Helenowski, M. Gopalakrishnan, D. Cutright, E. D. Donnelly, J. B. Strauss, Determining the organ at risk for lymphedema after regional nodal irradiation in breast cancer. *Int. J. Radiat. Oncol. Biol. Phys.* **105**, 649–658 (2019).
10. B. Wan, C. Ganier, X. Du-Harpur, N. Harun, F. Watt, R. Patalay, M. Lynch, Applications and future directions for optical coherence tomography in dermatology. *Br. J. Dermatol.* **184**, 1014–1022 (2021).
11. J.-L. Gennisson, T. Deffieux, M. Fink, M. Tanter, Ultrasound elastography: Principles and techniques. *Diagn. Interv. Imaging* **94**, 487–495 (2013).
12. M. Y. Jaffrin, H. Morel, Body fluid volumes measurements by impedance: A review of bioimpedance spectroscopy (BIS) and bioimpedance analysis (BIA) methods. *Med. Eng. Phys.* **30**, 1257–1269 (2008).
13. P. Clements, P. Lachenbruch, J. Seibold, B. Zee, V. Steen, P. Brennan, A. Silman, N. Allegar, J. Varga, M. Massa, Skin thickness score in systemic sclerosis: An assessment of interobserver variability in 3 independent studies. *J. Rheumatol.* **20**, 1892–1896 (1993).
14. B. Müller, L. Ruby, S. Jordan, M. B. Rominger, E. Mazza, O. Distler, Validation of the suction device Nimble for the assessment of skin fibrosis in systemic sclerosis. *Arthritis Res. Ther.* **22**, 128 (2020).
15. F. Hendriks, D. Brokken, J. Van Eemeren, C. Oomens, F. Baaijens, J. Horsten, A numerical-experimental method to characterize the non-linear mechanical behaviour of human skin. *Skin Res. Technol.* **9**, 274–283 (2003).
16. T. Virén, J. T. Iivarinen, J. K. Sarin, I. Harvima, H. N. Mayrovitz, Accuracy and reliability of a hand-held in vivo skin indentation device to assess skin elasticity. *Int. J. Cosmet. Sci.* **40**, 134–140 (2018).
17. Z. Ivanova, T. Aleksiev, H. Dobrev, N. Atanasov, Use of a novel indentometer to evaluate skin stiffness in healthy and diseased human skin. *Skin Res. Technol.* **29**, e13384 (2023).
18. H. Hu, Y. Ma, X. Gao, D. Song, M. Li, H. Huang, X. Qian, R. Wu, K. Shi, H. Ding, M. Lin, X. Chen, W. Zhao, B. Qi, S. Zhou, R. Chen, Y. Gu, Y. Chen, Y. Lei, C. Wang, C. Wang, Y. Tong, H. Cui, A. Abdal, Y. Zhu, X. Tian, Z. Chen, C. Lu, X. Yang, J. Mu, Z. Lou, M. Eghtedari, Q. Zhou, A. Oberai, S. Xu, Stretchable ultrasonic arrays for the three-dimensional mapping of the modulus of deep tissue. *Nat. Biomed. Eng.* **7**, 1321–1334 (2023).
19. C. Dagdeviren, Y. Shi, P. Joe, R. Ghaffari, G. Balooch, K. Usgaonkar, O. Gur, P. L. Tran, J. R. Crosby, M. Meyer, Y. Su, R. C. Webb, A. S. Tedesco, M. J. Slepian, Y. Huang, J. A. Rogers, Conformal piezoelectric systems for clinical and experimental characterization of soft tissue biomechanics. *Nat. Mater.* **14**, 728–736 (2015).
20. E. Song, Z. Xie, W. Bai, H. Luan, B. Ji, X. Ning, Y. Xia, J. M. Baek, Y. Lee, R. Avila, H.-Y. Chen, J.-H. Kim, S. Madhvapathy, K. Yao, D. Li, J. Zhou, M. Han, S. M. Won, X. Zhang, D. J. Myers, Y. Mei, X. Guo, S. Xu, J.-K. Chang, X. Yu, Y. Huang, J. A. Rogers, Miniaturized electromechanical devices for the characterization of the biomechanics of deep tissue. *Nat. Biomed. Eng.* **5**, 759–771 (2021).
21. C. Li, H. Wang, Z. Song, W. Zhang, Y. Pan, Z. Zhao, C. Qiu, K. Yin, M. Han, A. B. Wang, H. Luan, J. Li, W. Yan, S. Chen, H. Shen, T.-L. Liu, S. S. M. Lee, W. Ding, Y. Huang, J. A. Rogers, C. Wu, X. Ni, Wireless, wearable elastography via mechano-acoustic wave sensing for ambulatory monitoring of tissue stiffness. *Sci. Adv.* **11**, eady0534 (2025).
22. Y. Wang, J. Henderson, P. Hafiz, P. Turlapati, D. Ramsgard, W. Lipman, Y. Liu, L. Zhang, Z. Zhang, B. Davis, Z. Guo, S. Wang, L. Seymour, W. Xie, W. Bai, Near-infrared spectroscopy–enabled electromechanical systems for fast mapping of biomechanics and subcutaneous diagnosis. *Sci. Adv.* **10**, eadq9358 (2024).
23. A.-C. Campbell, J. E. Baik, A. Sarker, S. Brown, H. J. Park, K. G. Kuonqui, J. Shin, B. L. Pollack, A. Roberts, G. Ashokan, J. Rubin, R. P. Kataru, J. H. Dayan, A. V. Barrio, B. J. Mehrara, Breast cancer–related lymphedema results in impaired epidermal differentiation and tight junction dysfunction. *J. Invest. Dermatol.* **145**, 85–97.e4 (2025).
24. C. Sroog, Polyimides. *Prog. Polym. Sci.* **16**, 561–694 (1991).
25. Z. Xie, D. Bai, J. Ma, C. Jing, M. Lu, Characterization of bilayer tissue moduli and thickness via eccentric rotating mass dynamics. *Appl. Mech. Rev.* **78**, 041001 (2026).
26. D. He, D. Malu, Y. Hu, A comprehensive review of indentation of gels and soft biological materials. *Appl. Mech. Rev.* **76**, 050802 (2024).
27. J.-T. Kim, H.-S. Shin, J.-Y. Yoo, R. Avila, Y. Huang, Y. H. Jung, J. E. Colgate, J. A. Rogers, Mechanics of vibrotactile sensors for applications in skin-interfaced haptic systems. *Extreme Mech. Lett.* **58**, 101940 (2023).
28. Y. H. Jung, J.-Y. Yoo, A. Vázquez-Guardado, J.-H. Kim, J.-T. Kim, H. Luan, M. Park, J. Lim, H.-S. Shin, C.-J. Su, R. Schloen, J. Trueb, J.-K. Chang, D. S. Yang, Y. Park, H. Ryu, H.-J. Yoon, G. Lee, H. Jeong, J. U. Kim, R. Avila, A. Akhtar, J. Cornman, T.-i. Kim, Y. Huang, J. A. Rogers, A wireless haptic interface for programmable patterns of touch across large areas of the skin. *Nat. Electron.* **5**, 374–385 (2022).
29. Y. Liu, M. Pharr, G. A. Salvatore, Lab-on-skin: A review of flexible and stretchable electronics for wearable health monitoring. *ACS Nano* **11**, 9614–9635 (2017).
30. X. Liang, S. A. Boppart, Biomechanical properties of in vivo human skin from dynamic optical coherence elastography. *IEEE Trans. Biomed. Eng.* **57**, 953–959 (2009).
31. N. Bogduk, *Clinical Anatomy of the Lumbar Spine and Sacrum* (Elsevier Health Sciences, 2005).
32. A. G. Warren, H. Brorson, L. J. Borud, S. A. Slavin, Lymphedema: A comprehensive review. *Ann. Plast. Surg.* **59**, 464–472 (2007).
33. International Society of Lymphology, The diagnosis and treatment of peripheral lymphedema. *Lymphology* **36**, 84–91 (2003).
34. N. Cau, M. Galli, V. Cimolin, A. Grossi, I. Battarin, G. Puleo, A. Balzarini, A. Caraceni, Quantitative comparison between the laser scanner three-dimensional method and the circumferential method for evaluation of arm volume in patients with lymphedema. *J. Vasc. Surg. Venous Lymphat. Disord.* **6**, 96–103 (2018).
35. F. Bhimani, M. McEvoy, Y. Chen, A. Gupta, J. Pastoriza, A. Cavalli, L. Obaid, C. Rachofsky, S. Fruchter, S. Feldman, Comprehensive strategies in breast cancer-related lymphedema prevention: Insights from a multifaceted program. *Front. Oncol.* **14**, 1418610 (2024).
36. H. Dal, K. Açıkgöz, Y. Badienia, On the performance of isotropic hyperelastic constitutive models for rubber-like materials: A state of the art review. *Appl. Mech. Rev.* **73**, 020802 (2021).
37. J. W. Baish, T. P. Padera, L. L. Munn, The effects of gravity and compression on interstitial fluid transport in the lower limb. *Sci. Rep.* **12**, 4890 (2022).
38. D. Khanna, D. E. Furst, P. J. Clements, Y. Allanore, M. Baron, L. Czirjak, O. Distler, I. Foeldvari, M. Kuwana, M. Matucci-Cerinic, M. Mayes, T. Medsger Jr., P. A. Merkel, J. E. Pope, J. R. Seibold, V. Steen, W. Stevens, C. P. Denton, Standardization of the modified Rodnan skin score for use in clinical trials of systemic sclerosis. *J. Scleroderma Relat. Disord.* **2**, 11–18 (2017).
39. Q. Y. Weng, A. B. Raff, J. M. Cohen, N. Gunasekera, J.-P. Okhovat, P. Vedak, C. Joyce, D. Kroshinsky, A. Mostaghimi, Costs and consequences associated with misdiagnosed lower extremity cellulitis. *JAMA Dermatol.* **153**, 141–146 (2017).
40. C. K. Sen, G. M. Gordillo, S. Roy, R. Kirsner, L. Lambert, T. K. Hunt, F. Gottrup, G. C. Gurtner, M. T. Longaker, Human skin wounds: A major and snowballing threat to public health and the economy. *Wound Repair Regen.* **17**, 763–771 (2009).
41. D. Solav, K. M. Moerman, A. M. Jaeger, K. Genovese, H. M. Herr, MultiDIC: An open-source toolbox for multi-view 3D digital image correlation. *IEEE Access* **6**, 30520–30535 (2018).
42. P. Kapur, M. Jensen, L. J. Buxbaum, S. A. Jax, K. J. Kuchenbecker, "Spatially distributed tactile feedback for kinesthetic motion guidance," in *2010 IEEE Haptics Symposium* (IEEE, 2010), pp. 519–526.
43. S. Natsiavas, Analytical modeling of discrete mechanical systems involving contact, impact, and friction. *Appl. Mech. Rev.* **71**, 050802 (2019).
44. A. Bedford, K. M. Liechti, *Mechanics of Materials* (Springer, 2020).
45. M. Methia, S. Bouzidi, A. Benslimane, M. Arfaoui, N. A. Hocine, Stress analysis of a thick-walled cylinder composed of incompressible hyperelastic materials subjected to internal and/or external pressure: Analytical and finite element analysis. *J. Rubber Res.* **27**, 115–126 (2024).
46. O. A. Shergold, N. A. Fleck, D. Radford, The uniaxial stress versus strain response of pig skin and silicone rubber at low and high strain rates. *Int. J. Impact Eng.* **32**, 1384–1402 (2006).
47. E. L. Carniel, A. Berardo, I. Toniolo, C. G. Fontanella, Incremental moduli of isotropic hyperelasticity and parameters identification: Polynomial, exponential and power law formulations. *Int. J. Solids Struct.* **321**, 113552 (2025).



**Acknowledgments**

**Funding:** J.-T.K. was supported by the Institute of Information and Communications Technology Planning and Evaluation (IITP) grant funded by the Korea government (MSIT) (IITP-RS-2025-02214780, Generative Haptics and Fine Response Inference for Flexible Tactile Interfaces); research to test the device with patients with lymphedema was supported by funding from the Robert H. Lurie Comprehensive Cancer Center of Northwestern University under the Translational Engineering Initiative. **Author contributions:** Writing—original draft: M.-S.J., H.-S.S., J.-T.K., J.L.J., and A.M.F. Conceptualization: M.-S.J., H.-S.S., J.L.J., C.R., E.O.O., F.W., J.-Y.Y., Y.H., A.M.F., and J.A.R. Investigation: M.-S.J., H.-S.S., S.J., J.K., K.-H.H., T.W.P., J.B., J.L., W.S., S.M., H.P., Y.C., C.R., E.O.O., B.C.G., F.W., A.M.F., and Y.H. Writing—review and editing: M.-S.J., J.-T.K., S.L., J.L.J., S.X., C.R., E.O.O., J.-Y.Y., Y.H., A.M.F., and J.A.R. Methodology: M.-S.J., H.-S.S., J.-T.K., S.L., K.-H.H., C.R., B.C.G., F.W., J.-Y.Y., Y.H., and A.M.F. Resources: E.O.O., S.M., Y.H., A.M.F., and J.A.R. Funding acquisition: J.L.J., A.M.F., and J.A.R. Data curation: M.-S.J., S.J., J.K., A.M.F., S.N.G., and B.C.G. Validation: M.-S.J., J.-T.K., J.K., J.L.J., J.L., C.R., E.O.O., B.C.G., and A.M.F. Supervision: J.L.J., C.R., Y.H., A.M.F., and J.A.R. Formal analysis: M.-S.J., S.L., S.X., Y.H., and A.M.F. Software: M.-S.J., H.-S.S., J.-T.K., J.K., and J.-Y.Y. Visualization: M.-S.J., H.-S.S., J.-T.K., J.K., and J.L. Project administration: J.L.J., C.R., B.C.G., Y.H., A.M.F., and J.A.R. **Competing**

**interests:** The authors declare that they have no competing interests. **Data, code, and materials availability:** All data and code needed to evaluate and reproduce the results in the paper are present in the paper and/or the Supplementary Materials. This study did not generate new materials.

Submitted 7 February 2026
Accepted 2 June 2026
Published 15 July 2026
10.1126/sciadv.aeg2631

ScienceAdvances

# A wearable biomechanical system for medical evaluation of soft tissue disorders

Min-Seung Jo, Hee-Sup Shin, Jin-Tae Kim, Shupeng Li, Sonwoo Jung, Jungyeon Kim, Tae Wan Park, Jodi L. Johnson, Carrie Richardson, Eseosa Olive Osaghae, Kyoung-Ho Ha, Hyosik Park, Josif Bozovic, Winnie Sung, Jaewon Lim, Sammer Marzouk, Yujin Choi, Sofia Natasha Guzman, Bridget Christina Groble, Shuai Xu, Fredrick Wigley, Jae-Young Yoo, Yonggang Huang, Ann Marie Flores, and John A. Rogers

*Sci. Adv.* **12** (29), eaeg2631. DOI: 10.1126/sciadv.aeg2631



*Science Advances* (ISSN 2375-2548) is published by the American Association for the Advancement of Science. 1200 New York Avenue NW, Washington, DC 20005. The title *Science Advances* is a registered trademark of AAAS.